

Three-dimensional simulations of distorted Black Holes. I. Comparison with axisymmetric results.

Karen Camarda⁽¹⁾ and Edward Seidel^(2,3,4)

⁽¹⁾ *Department of Astronomy and Astrophysics and Center for Gravitational Physics and Geometry, Pennsylvania State University, University Park, PA 16802*

⁽²⁾ *Max-Planck-Institut für Gravitationsphysik, Schlaatzweg 1, 14473 Potsdam, Germany*

⁽³⁾ *National Center for Supercomputing Applications, Beckman Institute, 405 N. Mathews Ave., Urbana, IL 61801*

⁽⁴⁾ *Departments of Astronomy and Physics, University of Illinois, Urbana, IL 61801*

(August 21, 2021)

We consider the numerical evolution of black hole initial data sets, consisting of single black holes distorted by strong gravitational waves, with a full 3D, nonlinear evolution code. These data sets mimic the late stages of coalescing black holes. We compare various aspects of the evolution of axisymmetric initial data sets, obtained with this 3D code, to results obtained from a well established axisymmetric code. In both codes we examine and compare the behavior of metric functions, apparent horizon properties, and waveforms, and show that these dynamic black holes can be accurately evolved in 3D. In particular we show that with present computational resources and techniques, the process of excitation and ringdown of the black hole can be evolved, and one can now extract accurately the gravitational waves emitted from the 3D Cartesian metric functions, even when they carry away only a small fraction ($\ll 1\%$) of the rest mass energy of the system. Waveforms for both the $\ell = 2$ and the much more difficult $\ell = 4$ and $\ell = 6$ modes are computed and compared with axisymmetric calculations. In addition to exploring the physics of distorted black hole data sets, and showing the extent to which the waves can be accurately extracted, these results also provide important testbeds for all fully nonlinear numerical codes designed to evolve black hole spacetimes in 3D, whether they use singularity avoiding slicings, apparent horizon boundary conditions, or other evolution methods.

04.25.Dm, 95.30.Sf, 97.60.Lf

I. INTRODUCTION

In a recent paper [1], we showed that full 3D, Cartesian coordinate simulations of (axisymmetric) distorted, dynamic black holes can be performed, and through a comparison with results obtained with an axisymmetric code, that the waveforms can be accurately obtained. Although with present resolutions the length of the simulations is limited to about $t \approx 40M_{ADM}$ (due to the use of singularity avoiding time slicings, as detailed below), these results represent a step forward towards obtaining useful waveforms from 3D numerical calculations that will be needed for detecting and analyzing signals buried in the data collected by gravitational wave observatories. The need for an increasingly complex sequence of such simulations leading to realistic coalescence calculations is great, as gravitational wave observatories may detect such waves in about five years [2]. As black hole collisions are presently considered a most likely source of signals to be detected initially by these observatories, it is crucial to have a detailed theoretical understanding of the coalescence process that can only be achieved through numerical simulation [3,4]. In particular, it is most important to be able to simulate accurately the excitation of the coalescing black holes, to follow the waves generated in the process, and to extract gravitational waveforms

expected to be seen by detectors.

These are very difficult calculations, as one must simultaneously deal with singularities inside the black holes, follow the highly nonlinear regime in the coalescence process taking place near the horizons, and also calculate the linear regime in the radiation zone where the waves represent a very small perturbation on the background spacetime metric. The energy carried by these waves is typically found to be on the order of $10^{-6} - 10^{-2}M_{ADM}$. At such low amplitude, both the generation and propagation of these signals are susceptible to small numerical errors inherent in numerical simulations. Furthermore, one must numerically extract these waves from the metric functions actually being evolved, which in 3D are usually the Cartesian metric functions (e.g., g_{xx} , etc.). As these metric functions do not correspond directly to physical degrees of freedom, but rather to the gauge in which they are evolved, the determination of waves is provided by a complicated numerical procedure to isolate gauge-invariant waveforms (described below), which can introduce further numerical errors.

In axisymmetry, in the case of stellar collapse [5] or rotating collisionless matter [6] the evolution has been followed through black hole formation and emitted $\ell = 2$ waveforms have been studied. In this paper we focus on vacuum black holes, which exist in the initial data. Such

data sets are likely to be used in the fully general study of 3D black hole coalescence. Evolutions of vacuum black hole data sets have been carried out successfully for distorted black holes with rotation [7,8] and without [9,10], and for equal mass colliding black holes [11,12], but with difficulty. These 2D evolutions can be carried out to roughly $t = 100M_{ADM}$, where M_{ADM} is the ADM mass of the spacetime, although beyond this point large gradients related to singularity avoiding slicings usually cause the codes to become very inaccurate and crash. In full 3D, the simulations are more difficult as the numerical problems are exacerbated [13]. We will show examples of this difficulty in sections below.

These problems should be reduced through the use of apparent horizon boundary conditions (AHBC), that allow one to avoid the singularities not by pathological slicing conditions, but by excising the region inside the horizon. To date, impressive successes have been achieved in 1D [14–17], and also with spherical black holes in 3D [13,18,19]. But these techniques have not yet been applied to dynamic, nonspherical black hole systems. A completely different approach, using characteristic evolution, has recently been developed very successfully for 3D single black hole evolution, including distorted and rotating black holes [20], allowing extremely long term 3D evolutions for the first time. But for truly dynamic black holes evolved in 3D using any techniques (Cauchy evolution, Characteristic evolution, or AHBC), careful extraction of waveforms has been only recently been investigated in detail in Ref. [1]. Those results showed for the first time that the black hole ringdown dynamics, and the accompanying emission of low amplitude waves could be accurately computed in a full 3D simulation. Such results should be a useful testbed for techniques such as characteristic evolution and AHBC that enable long term black hole evolution.

In this paper we follow up on the results of Ref. [1] with a much more extensive and detailed examination of the evolution of axisymmetric black holes with a fully 3D code. These black hole initial data sets correspond to Schwarzschild initial data with a nonlinear gravitational wave superimposed, creating a distorted Schwarzschild system that will oscillate and settle down to a spherical hole with waves traveling out far from the hole. We show that with current techniques and computational resources available to 3D numerical relativity, distorted black holes can be evolved through the initial relaxation and part of the final ringdown period. We compare the evolution of metric functions and horizons obtained with an axisymmetric code written in spherical-polar coordinates using maximal slicing and a particular shift condition, to full 3D evolutions with a very general 3D code written in Cartesian coordinates, capable of using different slicing and shift conditions. We show that the gravitational waveforms can be followed and accurately extracted from the numerical evolutions, even though they

represent a small perturbation on the background spacetime which is also being evolved. We also study the extraction of fully *nonaxisymmetric* modes with the present code. In principle, of course, with axisymmetric initial data one should not excite nonaxisymmetric modes, but the extent to which they may be excited due to numerical effects in present codes needs to be investigated. We show below that numerical effects may excite such modes to some degree. This will provide important information when evolving true 3D, nonaxisymmetric black hole data sets, so that true signals can be clearly distinguished from numerical artifacts.

The extension of this work to full 3D black hole initial data, for which no testbeds exist at present, is in progress and will be published in the next paper in this series. In particular, nonaxisymmetric modes, such as the $\ell = 2, m = 2$ mode expected to be important in the ringing radiation for rotating black holes at late times [3], and therefore an important signal for gravitational wave observations, can now be studied [21–23].

The plan of the present paper is as follows. In section II we briefly review the initial data construction. In section III, we describe both the 2D and the 3D numerical codes used in the present simulations, and we study the numerical evolution of several representative distorted black hole data sets, discussing the behavior of metric functions, horizons, and waveforms extracted. In section IV we summarize and describe future work in this series.

II. INITIAL DATA

In this section we describe the axisymmetric initial data describing the distorted black holes to be evolved.

A. Mathematical construction and numerical implementation

There is by now a large body of literature on black hole initial data for numerical relativity. For multiple black holes, the early axisymmetric data sets of Misner [24] and Brill and Lindquist [25] were generalized to include spin and momentum by York and coworkers [26], culminating in the definitive work in 3D of Cook [27–29]. An alternate and simpler technique for computing multiple black hole initial data was recently developed by Brandt and Brügmann [30].

In this section we briefly describe the mathematical construction of initial data evolved in this paper, which constitute yet another family of black hole data sets for numerical relativity. These data sets are single, time symmetric, distorted black holes of the type studied in Refs. [31,32] as axisymmetric initial data, and their evolutions have been studied extensively in Ref. [9]. These

data sets have also been extended to include rotation [7,8,33], but we will not consider rotating black holes here. We will make extensive use of these data sets in our studies presented in this paper. They consist of a single black hole that has been distorted by the presence of an adjustable torus of nonlinear gravitational waves, of a form originally considered by Brill [34], which surrounds it. This is discussed in much more detail in Ref. [30], which focuses only on the initial data, where we study a broad family of full 3D distorted black holes, with and without rotation. We restrict ourselves here to nonrotating and axisymmetric cases, as studied previously in axisymmetry by [31]. The amplitude and shape of the torus of waves can be specified by hand, as described below, and can create very highly distorted black holes. For our purposes, we consider them as convenient initial data that create a distorted black hole that mimics the merger, just after coalescence, of two black holes colliding in axisymmetry [12].

Following [31], we write the 3-metric in the form originally used by Brill [34]:

$$d\ell^2 = \tilde{\psi}^4 (e^{2q} (d\eta^2 + d\theta^2) + \sin^2 \theta d\phi^2), \quad (1)$$

where η is a radial coordinate related to the standard Schwarzschild isotropic radius, which we refer to here as r , by

$$r = \frac{M}{2} e^\eta. \quad (2)$$

Then the η coordinate is related to the Cartesian coordinates by

$$\sqrt{x^2 + y^2 + z^2} = e^\eta. \quad (3)$$

(Here, and in what follows, we set the scale parameter M in [31] to be 2.) In spherical symmetry, if the “Brill wave” function q vanishes, the Schwarzschild initial data set results, as shown below, so for small values of the Brill wave one may regard this system as a perturbed black hole. For large waves, the black holes can become extremely distorted.

Given a choice for the “Brill wave” function q , the Hamiltonian constraint leads to an elliptic equation for the conformal factor $\tilde{\psi}$. (As these data sets are time symmetric, the momentum constraints are trivially satisfied. In Ref. [30] we consider the non-time symmetric case.) The function q represents the gravitational wave surrounding the black hole, and is chosen to be

$$q(\eta, \theta, \phi) = a \sin^n \theta \left(e^{-\left(\frac{\eta+b}{w}\right)^2} + e^{-\left(\frac{\eta-b}{w}\right)^2} \right) (1 + c \cos^2 \phi). \quad (4)$$

Thus, an initial data set is characterized by the parameters (a, b, w, n, c) , where, roughly speaking, a is the amplitude of the Brill wave, b is its radial location, w its

width, and c and the even integer n control its angular structure. Note that we have generalized the original axisymmetric construction to full 3D by the addition of the parameter c , but in this paper we restrict ourselves to $c = 0$ for comparison with axisymmetric results. A study of full 3D initial data and their evolutions will be published elsewhere [21,30].

If the amplitude a vanishes, the undistorted Schwarzschild solution results, leading to

$$\tilde{\psi} = 2 \cosh\left(\frac{\eta}{2}\right). \quad (5)$$

We note that just as the Schwarzschild geometry has an isometry that leaves the metric unchanged under the operation $\eta \rightarrow -\eta$, our data sets also have this property, even in the presence of the Brill wave. The radial point $\eta = 0$ is called the throat, as it is the surface that connects the identical geometries of two universes connected by an Einstein-Rosen bridge, or wormhole. As discussed in [13,35], this isometry condition can also be applied during the evolution and in Cartesian coordinates as well. We will make use of this condition in the work described in this paper.

As discussed in Ref. [30], we compute the initial data sets on a 3D grid in spherical coordinates, because the inner and outer boundaries are easier to handle. The outer boundary is a Robin condition, and the inner boundary is provided by the isometry condition described above. Once we have the conformal factor, we can specify the 3-metric, the form of which is given in Eq. (1). The extrinsic curvature vanishes, as these are time-symmetric initial data sets. Because of the higher resolution of the spherical grid in the inner regions, we found that computing derivatives of the conformal factor on this grid and storing the interpolated values on the Cartesian grid leads to more accurate evolution. Thus, we compute the first and second derivatives of the conformal factor $\tilde{\psi}$ with respect to the spherical coordinates (η, θ, ϕ) on the spherical grid.

For convenience, these manipulations are carried out on the spherical grid, but we perform evolutions in Cartesian coordinates. We have found it adequate to interpolate these quantities from the very fine 2D spherical grid onto the Cartesian grid using linear interpolation. With this information, we can perform simple coordinate transformations to convert these quantities to Cartesian coordinates obtaining:

$$\gamma_{ij} = \psi^4 \begin{pmatrix} \frac{y^2+x^2 e^{2q}}{x^2+y^2} & \frac{xy(e^{2q}-1)}{x^2+y^2} & 0 \\ \frac{xy(e^{2q}-1)}{x^2+y^2} & \frac{x^2+y^2 e^{2q}}{x^2+y^2} & 0 \\ 0 & 0 & e^{2q} \end{pmatrix}, \quad (6)$$

using the coordinate transformation implicit in Eq. (3). Finally, ψ and its Cartesian derivatives, computed via the coordinate transformation, are stored for use in computing “conformal” numerical derivatives, as described in Ref. [13].

Problem	a	n	M_{ADM}/M	M_{AH}/M	MRL
1	0.5	2	0.92	0.86	7.0×10^{-2}
2	0.5	4	0.97	0.92	6.0×10^{-2}
3	0.1	4	0.97	0.96	4.8×10^{-3}

TABLE I. We give the parameters for the three initial data sets from whose evolution we will present results in this paper. The complete set of black hole initial data parameters are (a, b, w, n, c) . The amplitude a and angular index n are given, while for all cases the Brill wave location and width parameters are $b = 0$, $w = 1$, and $c = 0$ indicating axisymmetric initial data. The quantity MRL is the maximum radiation loss possible during evolution for each data set, as discussed in the text. M is the scale parameter described in the text, taken to be 2 in this work.

B. Characteristics of sample initial data sets

In this section, we single out three initial data sets whose evolution and waveform emission are studied in detail in the following sections, and we present some of their physical characteristics before going on to evolutions.

In Table I, for each initial data set we give the ADM mass M_{ADM} , the apparent horizon mass M_{AH} , and the maximum radiation loss MRL , defined as in Ref. [31] as

$$MRL = \frac{M_{ADM} - M_{AH}(t=0)}{M_{ADM}}. \quad (7)$$

The MRL is an upper limit on the amount of energy the spacetime can emit as computed by considering the second law of black hole dynamics. The three cases studied range from slightly distorted, with an MRL of about $5 \times 10^{-3} M_{ADM}$, to highly distorted, with an MRL of $7 \times 10^{-2} M_{ADM}$. Problems 1 and 2 have the same distortion amplitude parameter, but different angular index n , leading to quite different ratios of $\ell = 4$ to $\ell = 2$ content in the initial data.

To give a visual picture of how distorted the black holes in these initial data sets are, we show the embedding of their apparent horizons. In Figs. 1, 2, and 3 we show the apparent horizon embeddings for Problems 1, 2, and 3, respectively. As shown previously in Ref. [31], black holes of this type with positive distortion amplitude a are have prolate horizons. Problem 3 is slightly perturbed, and nearly spherical, while Problems 1 and 2 are noticeably prolate. As in previous papers, we can characterize the shape of axisymmetric black holes with a single parameter: the polar to equatorial circumference ratio C_r . The horizons for Problems 1 and 2 are quite prolate, with $C_r = 2.7$ and 2.4 , respectively. Problem 2, with its angular index $n = 4$, actually has a “waist”, with negative Gaussian curvature in the region near the equator. Axisymmetric (2D) evolutions of similar data sets were studied extensively in Refs. [9,10,31], and dynamics of

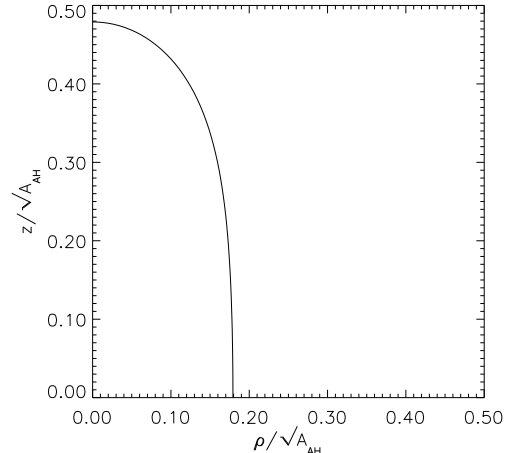


FIG. 1. We show the embedding of the apparent horizon for Problem 1, $(a, b, w, n, c) = (0.5, 0, 1, 2, 0)$. This black hole horizon is quite prolate, with a polar to equatorial circumference ratio $C_r = 2.7$.

the apparent and event horizons horizons of such data sets were detailed in [36–39].

These data sets will all go through oscillations, eventually settling down to become spherical Schwarzschild black holes as energy is radiated away. Note that Problems 1-3 form a sequence from most to least distorted, based on their horizon geometries, and also from largest to least possible radiation output, measured by their MRL . While Problem 3 is slightly distorted and a good candidate for study via perturbation theory, Problems 1 and 2 are fairly strongly distorted and are not well described by a first order perturbative treatment [22,23]. In the next section will study the full 3D evolution of these and other data sets in Cartesian coordinates.

III. EVOLUTION OF AXISYMMETRIC INITIAL DATA SETS

We now turn to the 3D evolution of the series of axisymmetric initial data sets described above. Comparisons of these results with those from well established 2D codes will help us confirm various aspects of the 3D results.

A. Numerical codes

1. 2D code

The code used to produce the 2D results in this paper is based on the one described in [35]. This code uses a logarithmic radial coordinate η related to the standard Schwarzschild isotropic radius r by $\eta = \ln(2r/M)$, where M is a scale parameter. As all data sets evolved with

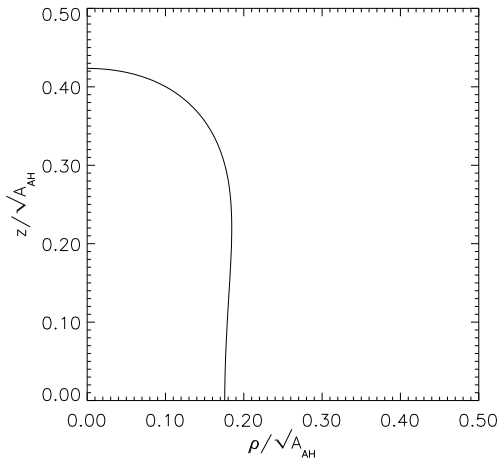


FIG. 2. We show the embedding of the apparent horizon for Problem 2, $(a, b, w, n, c) = (0.5, 0, 1, 4, 0)$. This horizon has a waist at the equator, with a polar to equatorial circumference ratio $C_r = 2.4$

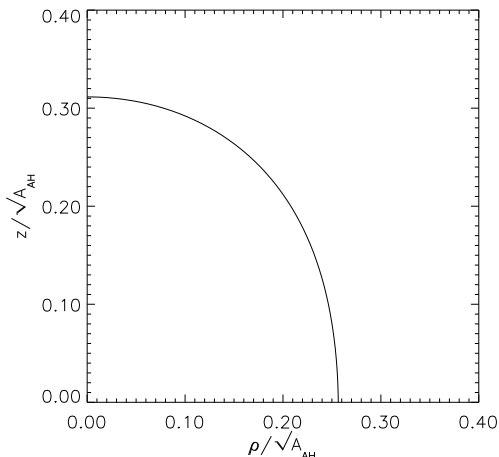


FIG. 3. We show the embedding of the apparent horizon for Problem 3, $(a, b, w, n, c) = (0.1, 0, 1, 4, 0)$. This slightly prolate horizon is the least distorted of the three Problems studied.

this code have equatorial-plane symmetry, the polar angle θ was restricted to lie between 0 and $\pi/2$ to decrease computational time. All 2D results presented were obtained using 200 radial zones and a maximum radius of $\eta_{max} = 6$, resulting in a radial grid spacing of $\Delta\eta = 0.03$. The number of angular zones, chosen to make $\Delta\theta \approx \Delta\eta$ was approximately 50.

The use of the logarithmic radial coordinate has the advantage of providing fine resolution near the throat of the black hole and also near the peak that develops in the radial metric function, while also allowing the outer boundary to be placed far from the hole. Disadvantages of this coordinate are that (i) The throat region remains extremely well resolved, even after the horizon has moved significantly away from the hole. Therefore much computational effort is wasted well inside the horizon where the lapse is typically near zero and the region is causally disconnected from the outside. (ii) The grid becomes very coarse outside the horizon in the radiation zone, because equal spacing in the η coordinate leads to larger and larger spacing in the more physical r coordinate. Under these conditions, waves may be reflected back toward the black hole as they are scattered off of the coarse grid at larger radii, as discussed in [9,35]. In fact, the effective Δr at the location of our wave extraction in the 2D code is approximately $0.45M$, which is typically much larger than the resolution of the 3D grid.

Except for the tests performed with geodesic slicing, the slicing used in the 2D code was maximal slicing. In order to stabilize the code along the axis, the shift vector is chosen to maintain the metric function $\gamma_{\eta\theta} = 0$, thus keeping constant-coordinate lines perpendicular ($\gamma_{\eta\phi}$ and $\gamma_{\theta\phi}$ also vanish). These details are extensively discussed in Refs. [10,35].

2. 3D code

a. The code. We developed a 3D code to study black holes and gravitational waves in Cartesian coordinates. This code (known as the ‘‘G’’ code) was applied to Schwarzschild black holes, where we showed that using singularity avoiding time slicings, a spherical black hole could be evolved accurately to $t = 30 - 50M$, depending on the resolution, location of the outer boundary, and the slicing conditions [13]. Beyond that time, the code generally crashes due to the unbounded growth of metric functions generated by singularity avoiding slicings. However, the focus of [13] was on spherical black holes, so no studies were made of black hole oscillations and the waves that would be generated in the process. It was shown that with spherical initial data some nonspherical behavior could be introduced by the Cartesian mesh and boundary conditions, the numerics of which could in principle generate spurious gravitational waves. This

3D code was then applied to the collision of two axisymmetric black holes (Misner data) [40], where we showed by comparison to 2D results that one could accurately track the merging of the horizons, and that the radiation emitted was qualitatively the same, but at that time the waveforms were not studied extensively. Building on the work presented in this paper and in Refs. [1,21], a more detailed study of the Misner data in 3D, including the waveforms, is in preparation for publication elsewhere.

The same code was simultaneously applied to the problem of pure gravitational waves [41,42], where many systems were studied, from pure linear quadrupole waves to nonlinear waves, and their propagation on a Cartesian mesh was studied. In that study it was shown that waves can be accurately evolved, although certain problems with gauge modes in the “near linear” regime that can confuse the results were identified, along with strategies to deal with them. Finally, the code has also been used to study coordinate conditions in 3D numerical relativity [43].

Based on this “G” code, we have developed a new version using the same numerical techniques, having similar convergence properties, etc., but rewritten to take advantage of newer parallel computer architectures, notably the SGI/Cray Origin 2000. We use the shared memory paradigm for parallelism in this code, avoiding the need to use a message passing library. With this model, we find both efficient single processor use and reasonably good scaling beyond 64 processors on the Origin 2000. The numerical techniques are as described in detail in [13]. We evolve the 3-metric and extrinsic curvature components with an explicit, staggered leapfrog scheme. For the algebraic slicing used to produce the results in this paper, described in the next section, the lapse function is evolved in this scheme as well.

b. Gauge conditions The 3D code has been written in a general way to accept general shift and slicing conditions. Although various shift conditions have been tested (e.g. minimal distortion shift as reported in Ref. [43] or an apparent horizon shift condition reported in Ref. [13]), in this work we restrict ourselves to the zero shift case. The application of different shift conditions to black hole spacetimes in 3D will be presented elsewhere.

We have experimented with a number of different slicing conditions. In Refs. [13,21] we discussed the use of geodesic slicing, maximal slicing and a host of algebraic slicing conditions for single and two black hole spacetimes. Geodesic slicing is useful only for performing certain tests of a code on a black hole spacetime. In brief, the slicing condition that worked the best for the analytic Schwarzschild and Misner two black hole spacetimes was the evolution of an initially maximal lapse, which vanishes on the throat of the black hole, with the “1+log” algebraic slicing. With this slicing condition we were able to produce accurate and stable evolutions for a period of time long enough to study the ringdown of excited black

holes, and it is much more computationally efficient than maximal slicing.

However, for the numerically generated distorted black hole initial data sets there is no appropriate analytic antisymmetric (i.e. vanishing on the throat) initial lapse to use, so we compute an antisymmetric maximal lapse numerically. Because it is inconvenient to compute and antisymmetric lapse across the black hole throat (which is a coordinate sphere) in the Cartesian coordinates with our elliptic solver, we compute the antisymmetric maximal lapse on the spherical grid and interpolate that onto the Cartesian grid. We have shown that this procedure when applied to the Schwarzschild case produces the same results as when the analytic Schwarzschild lapse is used, although it is necessary to use at least quadratic interpolation. This initial lapse is then evolved with the algebraic “1+log” lapse as described in Ref. [13]. This is the slicing condition used in all runs in this paper.

c. Computational domain and boundaries For the outer boundary, we presently hold the metric functions fixed in time. If the boundary is placed too close, this can have a serious effect on the behavior of waveforms and metric functions, and hence the largest possible computational domain is desirable. For evolutions of $30 - 50M$, typically we need to place the outer boundary at least as far as $20 - 25M$. The inner boundary (on the throat) is provided by an isometry condition, as described above.

Although the 3D evolution code is written without making use of any symmetry assumptions, the initial data we evolve in this paper have both equatorial plane symmetry and axisymmetry. Hence we save on the memory and computation required by evolving only one octant of the system. As shown in [13], this has no effect on the simulations except to reduce the computational requirements by a factor of eight. Even with such computational savings, these can be extravagant calculations. Smaller simulations presented in this paper have resolutions of typically 100^3 , and can easily be computed in a few hours on a 32 processor Origin 2000 at AEL. The highest resolution results presented in this paper were computed on a 3D Cartesian grid of 300^3 numerical grid zones, which is about a factor three larger than the largest production relativity calculations of which we are aware (which were about 200^3 zones). With our new code, these take about 12 Gbytes of memory, and require about a day on a 128 processor, early access Origin 2000 supercomputer at NCSA. These calculations were carried out in the summer of 1997 and winter of 1998.

B. Metric functions

In this section we make direct comparison between the quantities actually being evolved in both the 2D and 3D codes: metric functions. This provides a direct test of the evolutions of the same initial data sets in completely

different codes, coordinate systems, and in the 3D case, without enforcing symmetries required in the 2D code.

1. Geodesic slicing

We start by considering evolutions of axisymmetric initial data sets with geodesic slicing ($\alpha = 1$). For Schwarzschild, it is well known that in geodesic slicing a point initially on the throat will fall into the singularity at a time $t = \pi M$, and hence does not allow long term evolutions. For distorted black holes such as these, the results will differ somewhat from this analytic result, but the basic picture is the same. As shown in Ref. [13] geodesic slicing provides a powerful tests of the evolution equations. For these distorted black holes, it allows us to compare evolved metric functions with those obtained from a 2D code without the complication of a lapse calculation.

In Fig. 4 we show a plot of the conformal metric function $\hat{\gamma}_{rr} = \gamma_{rr}/\psi^4$ obtained from 2D and 3D codes along the z -axis for the distorted black hole initial data set $(a, b, w, n, c) = (0.5, 0, 1, 2, 0)$. Although the Cartesian metric functions are the ones actually evolved, we reconstruct the spherical metric functions numerically. Furthermore, dividing out the time independent conformal factor shows the dynamics more clearly. It is important to stress that the 2D data were obtained from an axisymmetric code that uses the logarithmic radial coordinate η . As discussed in section (III A 1), this has the effect of providing very high resolution near the throat, unlike in the 3D case. The 3D data were obtained using 70^3 grid points and a resolution of $\Delta x = 0.0543M_{ADM}$. In Fig. 5 we show a comparison of $\hat{\gamma}_{\theta\theta}/r^2$ from the two codes for the same runs. In both plots we see that the metric functions line up reasonably well. The small differences can easily be explained by the better resolution that is present in the 2D code, as discussed above.

The data in Figs. 4 and 5 are only shown to a time of $t = 0.977M_{ADM}$. The reason for this is not that the throat observers have already fallen into the singularity at that time. In fact, the 3D code with that resolution can be run past $t = 1.95M_{ADM}$ without developing problems. The problem is that the 2D code uses the standard spherical polar coordinate system, which has a coordinate singularity on the axis. Although there are no grid points actually on the axis, the code becomes unstable for grid points near the axis, causing the 2D code to crash very early. This problem is usually solved by using the gauge freedom of the Einstein equations to use the shift vector to maintain the metric function $\gamma_{r\theta} = 0$, thus keeping constant-coordinate lines perpendicular. However, the use of a non-zero shift results in a different 3-metric than in the vanishing shift case. Because this shift condition is not convenient to implement in the 3D Cartesian code, we were forced to compare with the zero-shift case, where

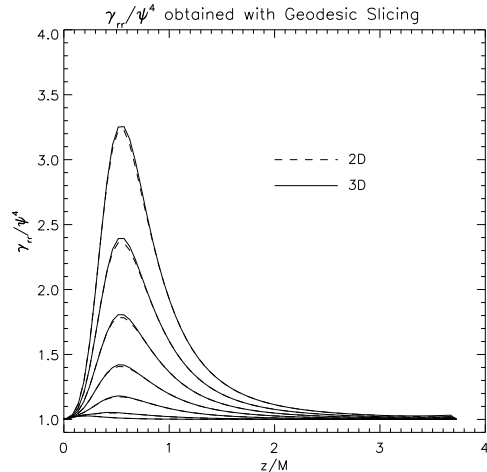


FIG. 4. We show a comparison of γ_{rr}/ψ^4 obtained with 2D and 3D codes using geodesic slicing. The data are shown every $0.163M_{ADM}$, to a maximum time of $t = 0.977M_{ADM}$. The 3D data were obtained with 70^3 grid points with a resolution of $\Delta x = 0.0543M_{ADM}$. The data set evolved was $(a, b, w, n) = (0.5, 0, 1, 2)$ (Problem 1).

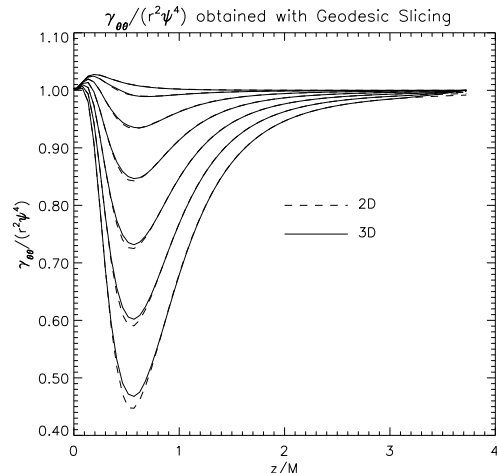


FIG. 5. As in Fig. 4, except that we plot $\gamma_{\theta\theta}/(r^2\psi^4)$. The data are shown at the same times as in Fig. 4.

the 2D code develops an axis instability when the evolution becomes very dynamic there.

To summarize the results of this section, we have carefully compared the evolutions of black hole initial data, in geodesic slicing, with both 2D and 3D codes. This provides a good test of the behavior of the code in the strong field regions near the horizon and singularity. In spite of the difficulties of evolution in 3D, in this case the 3D evolution is more robust than the 2D case due to an axis instability.

2. Singularity avoiding slicings

We next consider evolutions with the “1+log” slicing condition. The initial lapse is obtained as described above in section III A 2. Here we only show that the metric functions obtained are qualitatively the same in the two different codes. We cannot compare directly with data from 2D simulations, again because of the different slicing and shift conditions used.

As an example, we consider the evolution of the initial data set $(a, b, w, n, c) = (0.5, 0, 1, 2, 0)$ (Problem 1). This data set has an ADM mass of $M_{ADM} = 0.919M$. The run was done with 150^3 grid points with a resolution of $\Delta x = 0.0544M_{ADM}$. In Fig. 6a, we show the metric function $\hat{\gamma}_{rr}$ in the $x = 0$ plane at the time $t = 27.2M_{ADM}$. We see the characteristic peak growing in this metric function, caused by the differential acceleration of grid points towards the hole. The shape of the metric function is similar to that obtained with the 2D code. As in the Schwarzschild case, the peak growing near the origin is a result of the application of the isometry condition. In Fig 6b, we show the lapse function in the $x = 0$ plane at the same time. We see that, as in the Schwarzschild and Misner cases, the lapse which was initially antisymmetric at the throat, and evolved with “1+log” slicing, has collapsed at and around the throat.

The metric functions of the other black hole spacetimes studied in this paper behave similarly, and the comparisons with 2D results reveal the same qualitative agreement as expected.

C. Horizons

In this section we show a comparison of the location of the apparent horizon (AH), computed in the 3D and 2D codes. We computed the location of the AH during an evolution of the initial data set $(a, b, w, n, c) = (-0.5, 0, 1, 2, 0)$. The calculation was performed with 66^3 grid points with a resolution of $\Delta x = 0.2 = 0.056M_{ADM}$. For this run, maximal slicing was used. The AH was found using the 3D AH finder detailed in Ref. [44]. This

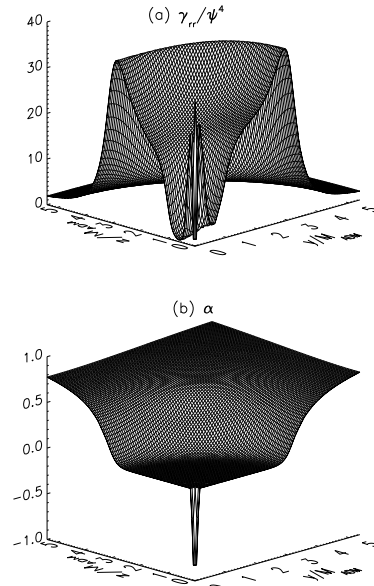


FIG. 6. We show (a) the conformal metric function $\hat{\gamma}_{rr}$ and (b) the lapse function α in the $x = 0$ plane for the evolution of the initial data set $(a, b, w, n, c) = (0.5, 0, 1, 2, 0)$ (Problem 1). The data shown are at a time of $t = 27.2M_{ADM}$. The evolution was run on a 150^3 grid, although data from only the inner 100^3 point are shown. The resolution was $\Delta x = 0.0544M_{ADM}$.

AH finder is implemented in full 3D, based on an expansion of the 2D horizon surface in symmetric trace free tensors.

Fig. 7 shows the horizon shapes and locations in the 3D calculation every $1.15M_{ADM}$ in time, starting at $t = 0$. The multipole order used in this calculation is $\ell = 4$, with only axisymmetric terms considered to reduce the computational time. The higher order expansion is needed here to describe the oblate shape of the horizons. Also shown in Fig. 7 are the corresponding surfaces found in our 2D axisymmetric code. We note that the slicing and shift conditions differ in the two cases, so we do not expect the surfaces to coincide precisely. In and around the $x - y$ plane, the solutions match to within half a grid cell. Greater differences, however, are found along the z -axis, where the two surfaces are displaced by a maximum of roughly two grid cells. This is attributed in part to a bigger $\Delta\alpha$ (~ 0.1) near the z -axis, which results from the imposed asymmetry in the lapse function due to the nearness of the outer boundaries, where we enforce the spherical Schwarzschild lapse as a boundary condition in the maximal equation used in the 2D simulation.

A more geometrical comparison or test of the solver is the mass of the surface found. The horizon mass is defined as $M_{AH} = \sqrt{A_{AH}/16\pi}$, where A_{AH} is the area of the surface. Fig. 8 plots the AH mass as a function of time for the 2D and the $\ell = 4$, 3D evo-

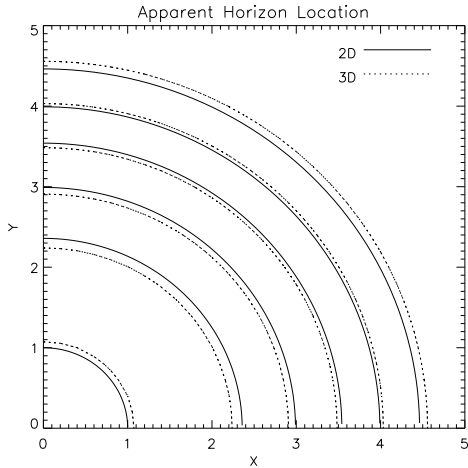


FIG. 7. Coordinate location of the AH found in the 2D and 3D evolutions of the initial data set $(a, b, w, n, c) = (-0.5, 0, 1, 2, 0)$. The surfaces are shown starting at $t = 0$ with time intervals of $1.12M_{ADM}$. Although we do not expect identical results due to different kinematic conditions in the two cases, the surfaces differ at most by little more than two grid cells. The evolution is performed on a 66^3 grid with $\Delta x = 0.2$.

lutions. In both cases, the mass increases at first, as the gravitational waves fall into the black hole, reaching $M_{AH} \sim 0.997M_{ADM}$ at $t \sim 6M_{ADM}$. The masses in the two cases differ by only 0.1% at $t \sim 6M_{ADM}$. For comparison we also plot M_{AH} for the surface found using a lower order $\ell = 2$ multipole expansion. At early times, when the horizon is most distorted, the $\ell = 2$ expansion is clearly not adequate to resolve the horizon shape, as evidenced by the AH mass which exceeds the ADM mass by about 1%. However, as the black hole settles down into a quasi-static state, the surface becomes more spherical and the $\ell = 2$ solution approaches both the 2D and the $\ell = 4$, 3D results, differing from the 2D result by about 0.35% at $t \sim 6M_{ADM}$.

D. Radiation extraction

Although in black hole simulations we evolve directly the metric and extrinsic curvature, for applications to gravitational wave astronomy we are particularly interested in computing the waveforms emitted. One measure of this radiation is the Zerilli function, ψ , which is a gauge-invariant function that obeys the Zerilli wave equation [45]. The Zerilli function can be computed by writing the metric as the sum of a spherically symmetric part and a perturbation: $g_{\alpha\beta} = \overset{o}{g}_{\alpha\beta} + h_{\alpha\beta}$, where the perturbation $h_{\alpha\beta}$ is expanded in tensor spherical harmonics. To compute the elements of $h_{\alpha\beta}$ in a numerical simulation, one integrates the numerically evolved metric components $g_{\alpha\beta}$ against appropriate spherical har-

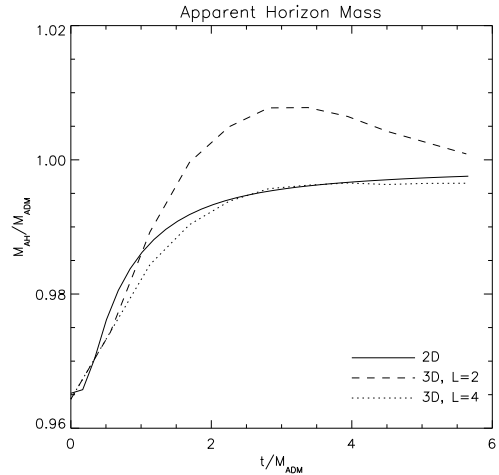


FIG. 8. Comparison of the apparent horizon masses computed from the 2D and 3D evolutions of the initial data set $(a, b, w, n, c) = (-0.5, 0, 1, 2, 0)$. The AH mass increases initially as the Brill wave falls into the black hole. By $t \sim 6M_{ADM}$, the mass approaches $0.997M_{ADM}$ and the 2D and $\ell = 4$, 3D results differ by just 0.1% at this time. We also show the corresponding masses computed from the surfaces found with an $\ell = 2$ multipole expansion. The low order expansion is clearly not adequate in resolving the surface at early times when the horizon is most distorted.

monics over a coordinate 2-sphere surrounding the black hole. The resulting functions can then be combined in a gauge-invariant way, following the prescription given by Moncrief [46]. This procedure was originally developed by Abrahams [47], and was applied to the same class of distorted black hole initial data sets discussed here, but evolved in 2D spherical-polar coordinates and with a different gauge, as discussed in [9].

1. 3D numerical implementation

We have developed numerical methods based on the same ideas to extract the waves in a full 3D Cartesian setting. The method used is essentially that used in the axisymmetric case, except that the metric functions and their spatial derivatives need to be interpolated onto a two-dimensional surface, which we choose to have constant coordinate radius. The projections of the perturbed metric functions $h_{\alpha\beta}$, and their radial derivatives, are then computed by numerically performing two-dimensional surface integrals for each $\ell - m$ mode desired. Then, for each mode, the Zerilli function is constructed from these projected metric functions, according to Moncrief's gauge-invariant prescription. This is a complicated but straightforward procedure.

a. Constructing the Zerilli Function As mentioned above, we assume the general metric can be decomposed into its spherical and non-spherical parts:

$$g_{\mu\nu} = \overset{\circ}{g}_{\mu\nu} + h_{\mu\nu}. \quad (8)$$

The spherical part $\overset{\circ}{g}_{\mu\nu}$ will of course be Schwarzschild, but we will in general not know the mass of this Schwarzschild background, or what coordinate system it will be in. However, in general, we know it can be written

$$\overset{\circ}{g}_{\mu\nu} = \begin{pmatrix} -N^2 & 0 & 0 & 0 \\ 0 & A^2 & 0 & 0 \\ 0 & 0 & R^2 & 0 \\ 0 & 0 & 0 & R^2 \sin^2 \theta \end{pmatrix} \quad (9)$$

where the functions N , A , and R are functions of our coordinate radius and time. Regge and Wheeler showed that $h_{\mu\nu}$ for even-parity perturbations (*i.e.*, perturbations which do not introduce angular momentum) can be written

$$h_{tt} = -N^2 H_0^{(\ell m)} Y_{\ell m} \quad (10)$$

$$h_{tr} = H_1^{(\ell m)} Y_{\ell m} \quad (11)$$

$$h_{t\theta} = h_0^{(\ell m)} Y_{\ell m, \theta} \quad (12)$$

$$h_{t\phi} = h_0^{(\ell m)} Y_{\ell m, \phi} \quad (13)$$

$$h_{rr} = A^2 H_2^{(\ell m)} Y_{\ell m} \quad (14)$$

$$h_{r\theta} = h_1^{(\ell m)} Y_{\ell m, \theta} \quad (15)$$

$$h_{r\phi} = h_1^{(\ell m)} Y_{\ell m, \phi} \quad (16)$$

$$h_{\theta\theta} = R^2 K^{(\ell m)} Y_{\ell m} + R^2 G^{(\ell m)} Y_{\ell m, \theta\theta} \quad (17)$$

$$h_{\theta\phi} = R^2 G^{(\ell m)} (Y_{\ell m, \theta\phi} - \cot \theta Y_{\ell m, \phi}) \quad (18)$$

$$h_{\phi\phi} = R^2 K^{(\ell m)} \sin^2 \theta Y_{\ell m} + R^2 G^{(\ell m)} (Y_{\ell m, \phi\phi} + \sin \theta \cos \theta Y_{\ell m, \theta}) \quad (19)$$

The spherical part of the metric, given in the functions N , A , and R , can be obtained by projecting the full metric against Y_{00} , yielding the following expressions*:

$$N^2 = -\frac{1}{4\pi} \int g_{tt} d\Omega \quad (20)$$

$$A^2 = \frac{1}{4\pi} \int g_{rr} d\Omega \quad (21)$$

$$R^2 = \frac{1}{8\pi} \int \left(g_{\theta\theta} + \frac{g_{\phi\phi}}{\sin^2 \theta} \right) d\Omega \quad (22)$$

Each ℓm -mode of $h_{\mu\nu}$ can then be obtained by projecting the full metric against the appropriate $Y_{\ell m}$. For example:

$$H_2^{(\ell m)} = \frac{1}{A^2} \int g_{rr} Y_{\ell m} d\Omega \quad (23)$$

Expressions for the other functions are provided in Ref. [22]. In practice, we do not extract A to compute $H_2^{(\ell m)}$, but rather we assume it to have the form $1 - \frac{2M}{R}$, where we take M to be the ADM mass of the spacetime. For the axisymmetric, equatorial plane symmetric, non-rotating initial data studied here, the only modes allowed are even-parity, even- ℓ modes.

Moncrief showed that the Zerilli function is gauge invariant, and can be constructed from the Regge-Wheeler variables as follows:

$$\psi^{(\ell m)} = \sqrt{\frac{2(\ell-1)(\ell+2)}{\ell(\ell+1)}} \frac{4RS^2 k_2^{(\ell m)} + \ell(\ell+1)Rk_1^{(\ell m)}}{\Lambda}, \quad (24)$$

where

$$\Lambda \equiv \ell(\ell+1) - 2 + \frac{6M}{R} \quad (25)$$

$$k_1^{(\ell m)} \equiv K^{(\ell m)} + SRG_{,R}^{(\ell m)} - 2\frac{S}{R}h_1^{(\ell m)} \quad (26)$$

$$k_2^{(\ell m)} \equiv \frac{H_2^{(\ell m)}}{2S} - \frac{1}{2\sqrt{S}} \frac{\partial}{\partial R} \left(\frac{RK^{(\ell m)}}{\sqrt{S}} \right) \quad (27)$$

$$S \equiv 1 - \frac{2M}{R}. \quad (28)$$

In order to compute the Regge-Wheeler perturbation functions h_1 , H_2 , G , and K , one needs the spherical metric functions on some 2-sphere. We get these by interpolating the Cartesian metric functions onto a surface of constant coordinate radius, and computing the spherical metric functions from these using the standard transformation. Second order interpolation is used. In order to compute the needed radial derivatives of these functions, we first compute the derivative of the Cartesian metric functions with respect to the coordinate radius on the Cartesian grid. We interpolate these quantities onto the 2-sphere. Then, to get the derivatives with respect to the Schwarzschild radius R , we use the derivative of Eq. (22) with respect to the coordinate r , giving

$$\frac{\partial R}{\partial r} = \frac{1}{16\pi R} \int \left(g_{\theta\theta, r} + \frac{g_{\phi\phi, r}}{\sin^2 \theta} \right) d\Omega. \quad (29)$$

The points on the 2-sphere to which we interpolate lie on lines of constant θ and ϕ , staggered across the coordinate axes. Integrations over each of these variables is performed with the second-order accurate Simpson's rule. Currently, 300 points are used for each angular coordinate. The numerical interpolations involved in this extraction procedure were also chosen to be second order accurate. Testing shows that both the interpolations and integrations do converge to second order in the relevant grid spacing.

We are aware of two possible improvements on this scheme. First, in the θ -integration, we could integrate

*We thank Gabrielle Allen for pointing out the error in the expression for R^2 in reference [9].

over $\cos\theta$ instead of θ . This could make these integrations more accurate, and would allow us to use fewer points, making the code more efficient. Second, we could interpolate onto a stereographic patch. This would distribute the points more evenly on the surface.

As in Ref. [9], we choose to normalize the Zerilli function so that the asymptotic energy flux in each mode is given by

$$\dot{E} = (1/32\pi)\dot{\psi}^2. \quad (30)$$

This assumes that linear theory is adequate to treat each individual mode. However, it is possible that in some regimes linear theory is *not* adequate, and hence the true energy calculation would require additional terms. The treatment of second order perturbation theory of this sort, including a derivation of the energy formula including higher order corrections, has been developed in Ref. [48].

Such considerations are actually relevant for the some of the initial data sets described here. For example, Problem 1 has angular parameter $n = 2$. One can show [30] that in an expansion of the initial data for small amplitude a , one recovers the Schwarzschild background with nonspherical perturbations, as assumed above. However, for $n = 2$, the series expansion in the amplitude parameter a brings in the $\ell = 2$ perturbations at linear order, but $\ell = 4$ does not appear until second order in a . Therefore, in order to be fully self-consistent the evolution equations for the $\ell = 4$ modes should actually be treated to second order, which implies that there should be nonlinear source terms coming from other linear modes (in this case, $\ell = 2$) in a consistent perturbation expansion, as discussed in Ref. [48]. Basically, in such cases the $\ell = 4$ mode is so small, that nonlinear contributions from other modes are not to be neglected. This need not concern us, because the evolutions considered in this paper are carried out fully nonlinearly, but it does mean that the interpretation, and in particular the calculation of the energy carried by a mode, must be carefully considered. Perturbative calculations, with comparisons to full nonlinear simulations, are in progress and will be reported elsewhere [22,23].

In the results discussed below, in cases where second order corrections should be considered in principle, we will continue to use the linear energy formula as a non-rigorous indication of the strength of a signal. The cases in question concern the $\ell > n$ modes (e.g., $\ell = 6$ in all cases and $\ell = 4$ for the $n = 2$ simulations, where n is the angular index of the Brill wave.)

To summarize this section, we have developed a general technique to extract the 3D waves propagating on a black hole background. There are cases where linear theory must be used with caution. While previously only axisymmetric simulations have been studied, we can now study all non-trivial wave modes, including those with $m \neq 0$.

2. Waveforms from 3D simulations of distorted black holes

In this section, we examine the waveforms for the three test cases described in detail above. This is a detailed followup to Ref. [1], so we present $\ell = 2$ and $\ell = 4$ waveforms for Problem 1 as before. We also consider two additional cases with different amplitudes and angular index n to show the fairly generic nature of these results. Finally, for the first time, we show that it is now possible in some cases to extract accurately even the $\ell = 6$ even-parity waveforms, both in the 2D and 3D cases, if the amplitude is not too small.

a. Problem 1. We extracted the $\ell = 2$ and $\ell = 4$ Zerilli functions during an evolution of the distorted black hole initial data set $(a, b, w, n, c) = (0.5, 0, 1, 2, 0)$, using the extraction method described above. In Fig. 9a we show the $\ell = 2$ Zerilli function extracted at a radius $r = 8.16M_{ADM}$ as a function of time. Superimposed on this plot is the same function computed during the evolution of the same initial data set with a 2D code, based on the one described in detail in [9,35]. The agreement of the two plots over the first peak is a strong affirmation of the 3D evolution code and extraction routine. It is important to note that the 2D results were computed with a different slicing (maximal), different coordinate system, and a *different spatial gauge*. Yet the physical results obtained by these two different numerical codes, as measured by the waveforms, are remarkably similar (as one would hope). This is a principal result of this paper. A full evolution with the 2D code to $t = 100M_{ADM}$, by which time the hole has settled down to Schwarzschild, shows that the energy emitted in this mode at that time is about $4 \times 10^{-3}M_{ADM}$. Therefore, although this was a highly distorted black hole, less than 5% of the *MRL* is actually radiated away. (Other modes are much smaller and do not contribute significantly to the total energy radiated.)

In Fig. 9b we show the $\ell = 4$ Zerilli function extracted at the same radius, computed during evolutions with 2D and 3D codes. This waveform is more difficult to extract, because it has a higher frequency in both its angular and radial dependence, and it has a much lower amplitude: using the linear theory formula discussed above (Eq. (30)) the energy emitted in this mode is three orders of magnitude smaller than the energy emitted in the $\ell = 2$ mode, *i.e.*, $10^{-6}M_{ADM}$, yet it can still be accurately evolved and extracted.

Small differences between the 2D and 3D results can be seen. Resolution studies of the 3D results indicate that the differences are not completely due to resolution of the 3D evolution code. The small differences in phase can be understood as a result of the different shift and slicings being used in the two simulations. The radiation is extracted at a constant *coordinate* location, and the coordinates fall towards the black hole at different

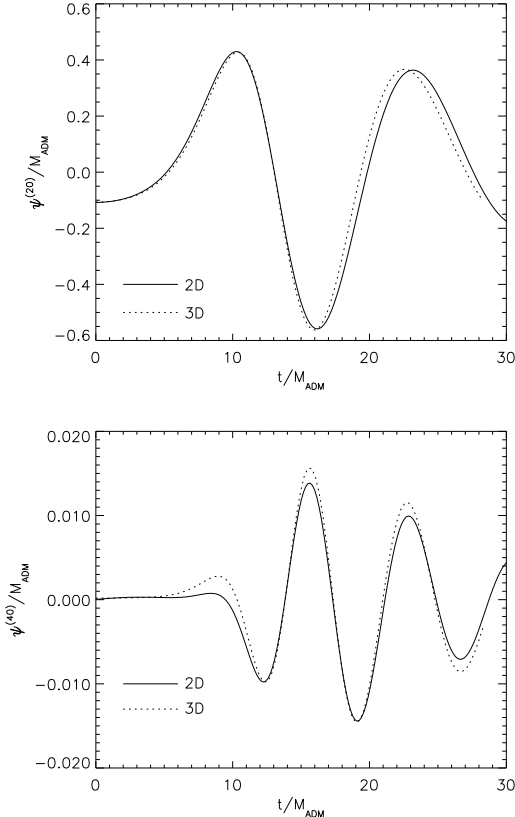


FIG. 9. We show the (a) $\ell = 2$, and (b) $\ell = 4$ Zerilli functions vs. time, extracted during 2D and 3D evolutions of the data set $(a, b, w, n, c) = (0.5, 0, 1, 2, 0)$ (Problem 1). The functions were extracted at a radius of $8.19M_{ADM}$. The 2D data were obtained with 202×54 grid points, giving a resolution of $\Delta\eta = \Delta\theta = 0.03$. The 3D data were obtained using 300^3 grid points and a resolution of $\Delta x = 0.109M_{ADM}$.

rates with different slicings and shifts. By measuring the physical radial position of the wave extraction in these simulations, we determined that the difference between the 2D and 3D phases at late time is consistent with the slightly different extraction locations in the two cases. The additional differences in the $\ell = 4$ waveforms could be related to slight differences in the initial data, which were generated in independent ways, or even differences in gauge (the waveforms are gauge-invariant, meaning they are unaffected only at first order under gauge transformations). As $\ell = 4$ has a much smaller amplitude than $\ell = 2$, it will be more sensitive to such details.

Since this data set is axisymmetric, the non-axisymmetric Zerilli functions of a perfect evolution should vanish. However, we expect that numerical errors, especially errors due to the distinctly non-axisymmetric outer boundary, will result in finite values for these Zerilli functions. Knowing the size of the error produced will help us gauge the accuracy of our results when we move to full 3D, where we expect real non-axisymmetric signals.

In Fig. 10, we show non-axisymmetric Zerilli functions as a function of time, extracted during an evolution of the same data set as above, at the same radius. We see that the $\ell = 2, m = 2$ and $\ell = 4, m = 2$ waveforms remain very small throughout the evolution. The $\ell = 4, m = 4$ waveform, while an order of magnitude smaller than the $\ell = 4, m = 0$ waveform, is still much larger than the other non-axisymmetric waveforms. Preliminary tests computing these quantities for Schwarzschild initial data, for which all Zerilli functions should vanish, indicate that the $\ell = 4, m = 4$ waveform is more sensitive to errors in the interpolation of metric functions onto the spherical extraction surface than the other Zerilli functions are. The reason for this sensitivity and how to correct for it are under investigation.

Resolution studies show that the waveforms are converging at roughly second order in the grid spacing. The axisymmetric $\ell = 2, 4$ modes have converged at the resolution shown, while the $\ell = m = 4$ mode is converging towards zero, although at the highest resolution we have computed it is still relatively large.

b. Problem 2 We now turn to Problem 2, which is similar to Problem 1, but with angular index $n = 4$. In this case the initial data contain a much larger $\ell = 4$ and $\ell = 6$ mode content. In this example, we extract the $\ell = 2, 4, 6$ modes during the 3D evolution, and compare with the 2D axisymmetric evolution. Fig. 11 shows the comparisons between the waveforms, showing that for this highly distorted black hole, even the $\ell = 6$ waveform computed in 3D agrees very well with the axisymmetric simulation. As in the previous case, we emphasize that these two calculations are done in different geometries, different slicing conditions, and different spatial gauges.

For this simulation, the total radiated energy carried in the $\ell = 2$ mode is $2 \times 10^{-3}M_{ADM}$, or about 3% of the

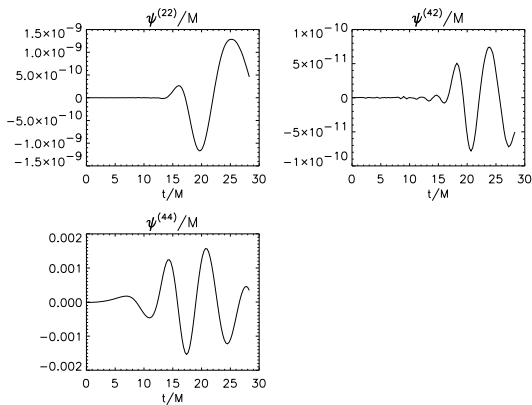


FIG. 10. We show the non-axisymmetric Zerilli functions as a function of time extracted during an evolution of the axisymmetric data set $(a, b, w, n, c) = (0.5, 0, 1, 2, 0)$ (Problem 1). The extraction was done at a radius of $r = 8.16M_{ADM}$. The calculation was performed with 300^3 grid points and a resolution of $\Delta x = 0.109M_{ADM}$.

MRL. The $\ell = 4$ mode carries $1 \times 10^{-4}M_{ADM}$ in energy, much larger than in the previous case. In this case the $\ell = 4$ mode is a first order perturbation in the Brill wave amplitude, and the linear energy calculation applies.

c. Problem 3 Finally, we study the waveforms extracted in Problem 3, which has a much lower distortion amplitude, and hence much weaker waves which are harder to evolve and extract accurately. In Fig. 12 we show the three waveforms. The $\ell = 2$ and $\ell = 4$ 3D waveforms agree well with those computed in 2D, as in previous cases. But the $\ell = 6$ waveform has an offset indicating some level of error in either the extraction or the evolution itself. In this simulation the $\ell = 6$ mode is about 20 times smaller than that extracted in Problem 2. If one examines the $\ell = 6$ waveform from Problem 2 closely, one can see a similar offset of the same level, but compared to the waveform in that case the effect is almost not noticeable. However, in Problem 3, with such a smaller amplitude signal, the offset can be seen readily. Resolution studies of this mode indicate that it is converging toward the 2D result as the resolution increases. But even at the highest 300^3 resolution, there is enough error to make extracting this very small signal (much smaller than any other modes presented) rather difficult. The reasons for the offset in $\ell = 6$ waveforms are under investigation.

The energy emitted in the $\ell = 2$ mode is $9 \times 10^{-5}M_{ADM}$, again, only a few per cent of the MRL. The energy emitted in the $\ell = 4$ mode is $6 \times 10^{-6}M_{ADM}$.

IV. CONCLUSIONS

In this followup paper to Ref. [1], we have performed the first detailed study of the dynamics of axisymmetric, distorted black holes with a general 3D code. This work

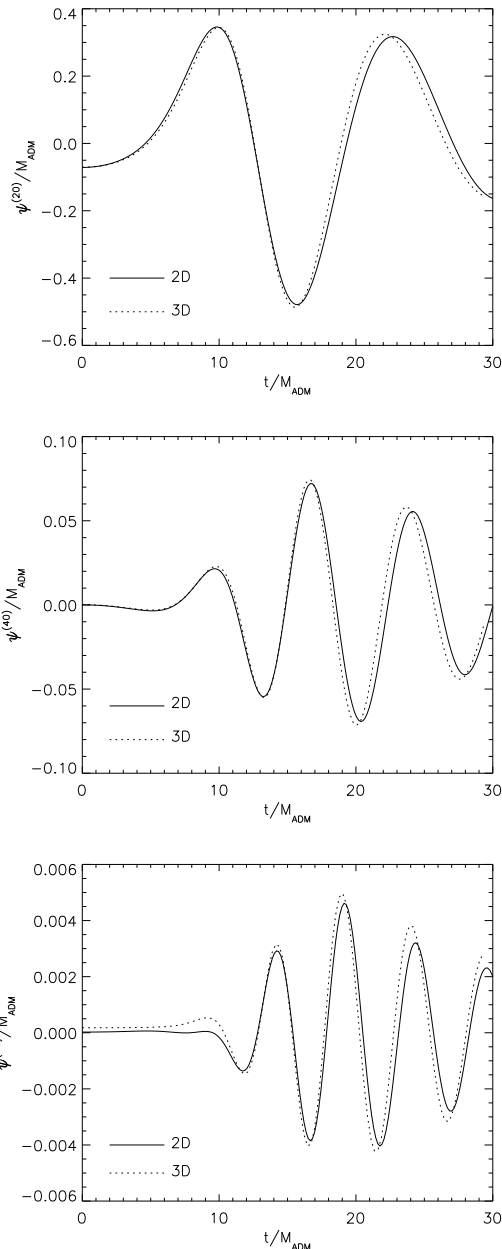


FIG. 11. We show the (a) $\ell = 2$, (b) $\ell = 4$, and (c) $\ell = 6$ Zerilli functions vs. time, extracted during 2D and 3D evolutions of the data set $(a, b, w, n, c) = (0.5, 0, 1, 4, 0)$ (Problem 2). The functions were extracted at a radius of $7.72M_{ADM}$. The 2D data were obtained with 202×54 grid points, giving a resolution of $\Delta\eta = \Delta\theta = 0.03$. The 3D data were obtained using 300^3 grid points and a resolution of $\Delta x = 0.103M_{ADM}$.

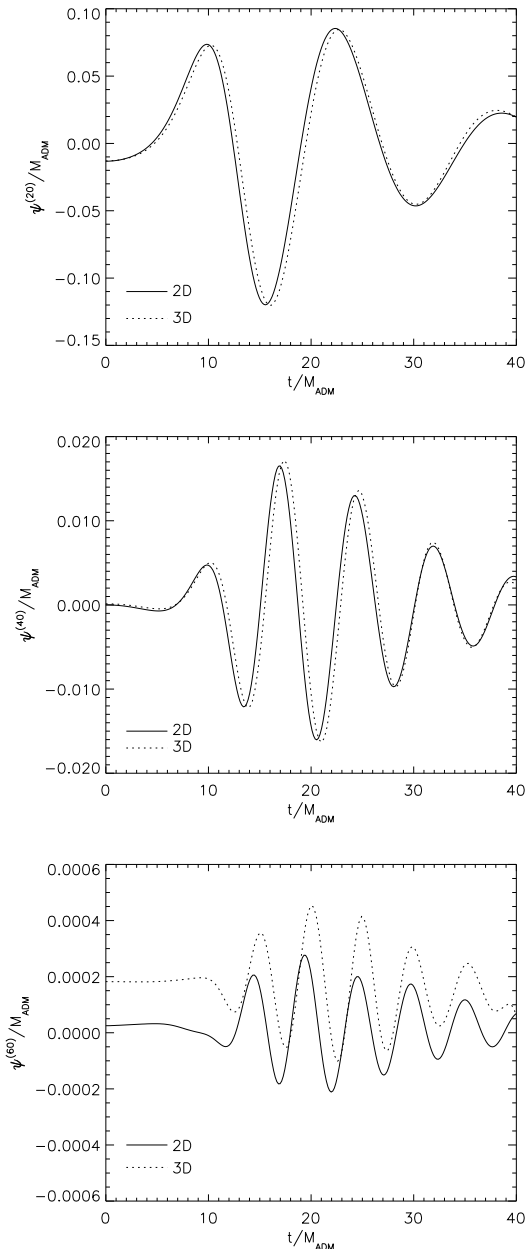


FIG. 12. We show the (a) $\ell = 2$, (b) $\ell = 4$, and (c) $\ell = 6$ Zerilli functions vs. time, extracted during 2D and 3D evolutions of the data set $(a, b, w, n, c) = (0.1, 0, 1, 4, 0)$ (Problem 3). The functions were extracted at a radius of $7.88M_{ADM}$. The 2D data were obtained with 202×54 grid points, giving a resolution of $\Delta\eta = \Delta\theta = 0.03$. The 3D data were obtained using 300^3 grid points and a resolution of $\Delta x = 0.104M_{ADM}$.

is another step in the development of 3D numerical relativity towards codes capable of simulating the spiraling coalescence of binary black hole systems. In this step, we have shown that, given sufficient resolution in 3D Cartesian coordinates, distorted black holes, which are used to model the late stages of binary black hole mergers just after the horizons have merged, can be accurately evolved. We studied the behavior of metric functions and apparent horizons in these spacetimes evolved in 3D Cartesian coordinates, and compared them with evolutions provided by 2D codes in polar-spherical coordinates, and showed that the results agree well.

Furthermore, we showed that the gravitational waveforms generated by the black hole, consisting of small perturbations on the evolving black hole background, can be accurately propagated and extracted from the numerically generated metric, on a 3D Cartesian grid. We have demonstrated this by comparing results from a mature 2D code, showing good agreement not only for the $\ell = 2$, but also with the higher $\ell = 4$ and even the $\ell = 6$ modes of the radiation, in cases where they are strong enough to stand above numerical error. Such modes are much weaker than the dominant $\ell = 2$ modes, and have much higher frequency and more complex angular dependence, yet they can be accurately tracked and resolved in full 3D. To our knowledge, this is the first study of $\ell = 6$ modes with any nonlinear evolution code.

Although we regard this as an important step in establishing numerical relativity as a viable tool to compute waveforms from black hole interactions, the calculations one can presently do are limited. With present techniques, the evolutions can only be carried out for a fraction of the time required to simulate the 3D orbiting coalescence. Many techniques to handle this more general case are under development, such as hyperbolic formulations of the Einstein equations and the advanced numerical methods they bring [49], adaptive mesh refinement that will enable placing the outer boundary farther away while resolving the strong field region where the waves are generated [50], and apparent horizon boundary conditions that excise the interiors of the black holes, thus avoiding the difficulties associated with singularity avoiding slicings [14,18,19].

In a completely different approach, a 3D code based on a characteristic formulation of the equations was shown to overcome some limitations of 3D Cauchy codes, to evolve distorted black holes for essentially unlimited times (more than $t \approx 60,000M$), on distorted black holes. Although it is not clear if characteristic evolution will be able to handle highly distorted or colliding black holes, it would be very interesting to study black hole systems such as these to see if the black hole ringdown and waveforms can be also be accurately extracted.

All of these techniques, and others, may be needed to handle the more general, long term evolution of coalescing black holes. Our purpose in this paper has been

to show that (a) given present resources one can evolve simpler distorted black hole systems and accurately extract the waveforms, even when they carry only $10^{-6}M$ in energy, and (b) to establish testbeds for the techniques under development for the more general case. Experience has shown that although the gross dynamics of black hole evolutions are fairly robust to different treatments in fully nonlinear codes, the waveforms are very sensitive and difficult to compute correctly [1,7–12,21,51]. Each of these new techniques may introduce numerical artifacts, even if at very low amplitude, to which the waveforms may be very sensitive. As new methods are developed and applied to numerical black hole simulations, they can now be tested on evolutions such as those presented here to ensure that the waveforms can be accurately computed.

In future papers we extend this work and apply it to full 3D initial data sets where nonaxisymmetric modes can be extracted for the first time [21,23,52], and to the evolution of colliding black holes in 3D, extending the work in [40]. Once these techniques have been fully developed and tested on true 3D data sets, it will be important to apply it to true 3D black hole collision simulations, such as those recently reported by Brüggmann [53].

ACKNOWLEDGMENTS

This work has been supported by the Albert Einstein Institute (AEI), NCSA, and the Binary Black Hole Grand Challenge Alliance, NSF PHY/ASC 9318152 (ARPA supplemented). We would like to thank K.V. Rao, John Shalf, and the staff at NCSA for assistance with the computations. Among many colleagues at NCSA, AEI, and Washington University who have influenced this particular work, we especially thank Andrew Abrahams, Gabrielle Allen, Larry Smarr, and Wai-Mo Suen. E.S. would like to thank Carles Bona and J. Massó for hospitality at the University of the Balearic Islands for hospitality while this manuscript was revised. Calculations were performed at AEI and NCSA on an SGI/Cray Origin 2000 supercomputer.

-
- [1] K. Camarda and E. Seidel, Phys. Rev. D **57**, R3204 (1998).
- [2] A. A. Abramovici *et al.*, Science **256**, 325 (1992).
- [3] É. É. Flanagan and S. A. Hughes, Phys. Rev. D **57**, 4535 (1998).
- [4] É. É. Flanagan and S. A. Hughes, Phys. Rev. D **57**, 4566 (1998).
- [5] R. F. Stark and T. Piran, Phys. Rev. Lett. **55**, 891 (1985).
- [6] A. M. Abrahams, G. B. Cook, S. L. Shapiro, and S. A. Teukolsky, Phys. Rev. D **49**, 5153 (1994).
- [7] S. Brandt and E. Seidel, Phys. Rev. D **52**, 856 (1995).
- [8] S. Brandt and E. Seidel, Phys. Rev. D **52**, 870 (1995).
- [9] A. Abrahams *et al.*, Phys. Rev. D **45**, 3544 (1992).
- [10] P. Anninos *et al.*, in *Computational Astrophysics: Gas Dynamics and Particle Methods*, edited by W. Benz, J. Barnes, E. Muller, and M. Norman (Springer-Verlag, New York, 1997), in press.
- [11] P. Anninos *et al.*, Phys. Rev. Lett. **71**, 2851 (1993).
- [12] P. Anninos *et al.*, Phys. Rev. D **52**, 2044 (1995).
- [13] P. Anninos *et al.*, Phys. Rev. D **52**, 2059 (1995).
- [14] E. Seidel and W.-M. Suen, Phys. Rev. Lett. **69**, 1845 (1992).
- [15] P. Anninos *et al.*, Phys. Rev. D **51**, 5562 (1995).
- [16] M. A. Scheel, S. L. Shapiro, and S. A. Teukolsky, Phys. Rev. D **51**, 4208 (1995).
- [17] R. Marsa and M. Choptuik, Phys Rev D **54**, 4929 (1996).
- [18] G. E. Daues, Ph.D. thesis, Washington University, St. Louis, Missouri, 1996.
- [19] G. B. Cook *et al.*, Phys. Rev. Lett. **80**, 2512 (1998).
- [20] R. Gomez *et al.*, Phys. Rev. Lett. **80**, 3915 (1998).
- [21] K. Camarda, Ph.D. thesis, University of Illinois at Urbana-Champaign, Urbana, Illinois, 1998.
- [22] G. Allen, K. Camarda, and E. Seidel, in preparation.
- [23] G. Allen, K. Camarda, and E. Seidel, in preparation.
- [24] C. Misner, Phys. Rev. **118**, 1110 (1960).
- [25] D. S. Brill and R. W. Lindquist, Phys. Rev. **131**, 471 (1963).
- [26] J. Bowen and J. W. York, Phys. Rev. D **21**, 2047 (1980).
- [27] G. Cook, Ph.D. thesis, University of North Carolina at Chapel Hill, Chapel Hill, North Carolina, 1990.
- [28] G. B. Cook, Phys. Rev. D **44**, 2983 (1991).
- [29] G. B. Cook *et al.*, Phys. Rev. D **47**, 1471 (1993).
- [30] S. Brandt, K. Camarda, and E. Seidel, in preparation.
- [31] D. Bernstein, D. Hobill, E. Seidel, and L. Smarr, Phys. Rev. D **50**, 3760 (1994).
- [32] D. Bernstein, Ph.D. thesis, University of Illinois Urbana-Champaign, 1993.
- [33] S. Brandt and E. Seidel, Phys. Rev. D **54**, 1403 (1996).
- [34] D. S. Brill, Ann. Phys. **7**, 466 (1959).
- [35] D. Bernstein *et al.*, Phys. Rev. D **50**, 5000 (1994).
- [36] P. Anninos *et al.*, Phys. Rev. D **50**, 3801 (1994).
- [37] P. Anninos *et al.*, IEEE Computer Graphics and Applications **13**, 12 (1993).
- [38] P. Anninos *et al.*, Phys. Rev. Lett. **74**, 630 (1995).
- [39] P. Anninos *et al.*, Australian Journal of Physics **48**, 1027 (1995).
- [40] P. Anninos, J. Massó, E. Seidel, and W.-M. Suen, Physics World **9**, 43 (1996).
- [41] P. Anninos *et al.*, Phys. Rev. D **56**, 842 (1997).
- [42] P. Anninos *et al.*, Phys. Rev. D **54**, 6544 (1996).
- [43] J. Balakrishna *et al.*, Class. Quant. Grav. **13**, L135 (1996).
- [44] P. Anninos *et al.*, gr-qc/9609059, (1998), to appear in Phys. Rev. D.
- [45] F. J. Zerilli, Phys. Rev. Lett. **24**, 737 (1970).
- [46] V. Moncrief, Annals of Physics **88**, 323 (1974).
- [47] A. Abrahams, Ph.D. thesis, University of Illinois, Urbana, Illinois, 1988.
- [48] R. J. Gleiser, C. O. Nicasio, R. H. Price, and J. Pullin,

Class. Quant. Grav. **13**, L117 (1996).

- [49] C. Bona, J. Massó, E. Seidel, and J. Stela, Phys. Rev. D **56**, 3405 (1997).
- [50] P. Papadopoulos, E. Seidel, and L. Wild, Phys. Rev. D (1998), submitted, gr-qc/9802069.
- [51] P. Anninos *et al.*, Technical Report No. 24, National Center for Supercomputing Applications (unpublished).
- [52] G. Allen, K. Camarda, and E. Seidel, in preparation.
- [53] B. Brügmann, gr-qc/9708035.